Ultrafast Plasmonic Nucleic Acid Amplification and Real-Time Quantification for Decentralized Molecular Diagnostics

Byoung-Hoon Kang, Kyung-Won Jang, Eun-Sil Yu, Hamin Na, Yun-Jae Lee, Woong-Yeol Ko, NamHo Bae, Donggee Rho, and Ki-Hun Jeong*

ACCESS | Metrics & More | Article Recommendations | SI Supporting Information

ABSTRACT: Point-of-care real-time reverse-transcription polymerase chain reaction (RT-PCR) facilitates the widespread use of rapid, accurate, and cost-effective near-patient testing that is available to the public. Here, we report ultrafast plasmonic nucleic acid amplification and real-time quantification for decentralized molecular diagnostics. The plasmonic real-time RT-PCR system features an ultrafast plasmonic thermocycler (PTC), a disposable plastic-on-metal (PoM) cartridge, and an ultrathin microlens array fluorescence (MAF) microscope. The PTC provides ultrafast photothermal cycling under white-light-emitting diode illumination and precise temperature monitoring with an integrated resistance temperature detector. The PoM thin film cartridge allows rapid heat transfer as well as complete light blocking from the photothermal excitation source, resulting in real-time and highly efficient PCR quantification. Besides, the MAF microscope exhibits close-up and high-contrast fluorescence microscopic imaging. All of the systems were fully packaged in a palm size for point-of-care testing. The real-time RT-PCR system demonstrates the rapid diagnosis of coronavirus disease-19 RNA virus within 10 min and yields 95.6% of amplification efficiency, 96.6% of classification accuracy for preoperational test, and 91% of total percent agreement for clinical diagnostic test. The ultrafast and compact PCR system can decentralize point-of-care molecular diagnostic testing in primary care and developing countries.

KEYWORDS: plasmonic PCR, real-time PCR, ultrafast molecular diagnostics, point-of-care test, photothermal effect, SARS-CoV-2
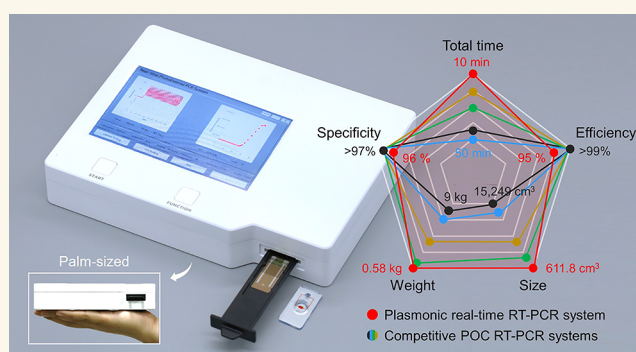
Decentralized diagnostic testing during the coronavirus disease 2019 (COVID-19) pandemic helps continuous screening of individuals at the site of patient care for timely recognition of infection and reduction of virus transmission.[1−3] Rapid, compact, and cost-effective point-of-care (POC) testing devices allow immediate clinical decision-making by providing narrowing spatial and temporal gaps between the diagnostic test and the clinical outcome.[4−6] However, rapid antigen immunoassays dominant in POC diagnostics have limited availability of definite diagnosis due to high false negative rate at an early disease stage.[7−9] As an alternative, reverse-transcription polymerase chain reaction (RT-PCR) plays a main role in molecular testing even outside the clinical laboratories for high diagnostic accuracy; however, it is impractical for the POC use due to time-consuming protocols, longstanding experience, and operational complexity.[10,11] In addition, conventional RT-PCR systems require technical advances for short turn-around time, compact system size, and low cost with overall reliability and robustness.[12]

Plasmonic photothermal effects of metallic nanomaterials provide creative inspiration for ultrafast amplification times.[5,13,14] For instance, the rapid PCR was achieved using laser-mediated volumetric heating from dispersed nanoparticles[15−22] or light-emitting diode (LED)-driven surface heating from large area nanostructures.[23−27] The plasmonic PCR often faces either nonspecific adsorption of PCR reagents to the nanomaterials or indirect temperature measurement, which substantially reduces the PCR efficiency.[28] Unlike the nanoparticles, the plasmonic nanostructures effectively isolate the PCR mixtures by thin-film passivation and also simplify
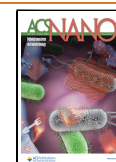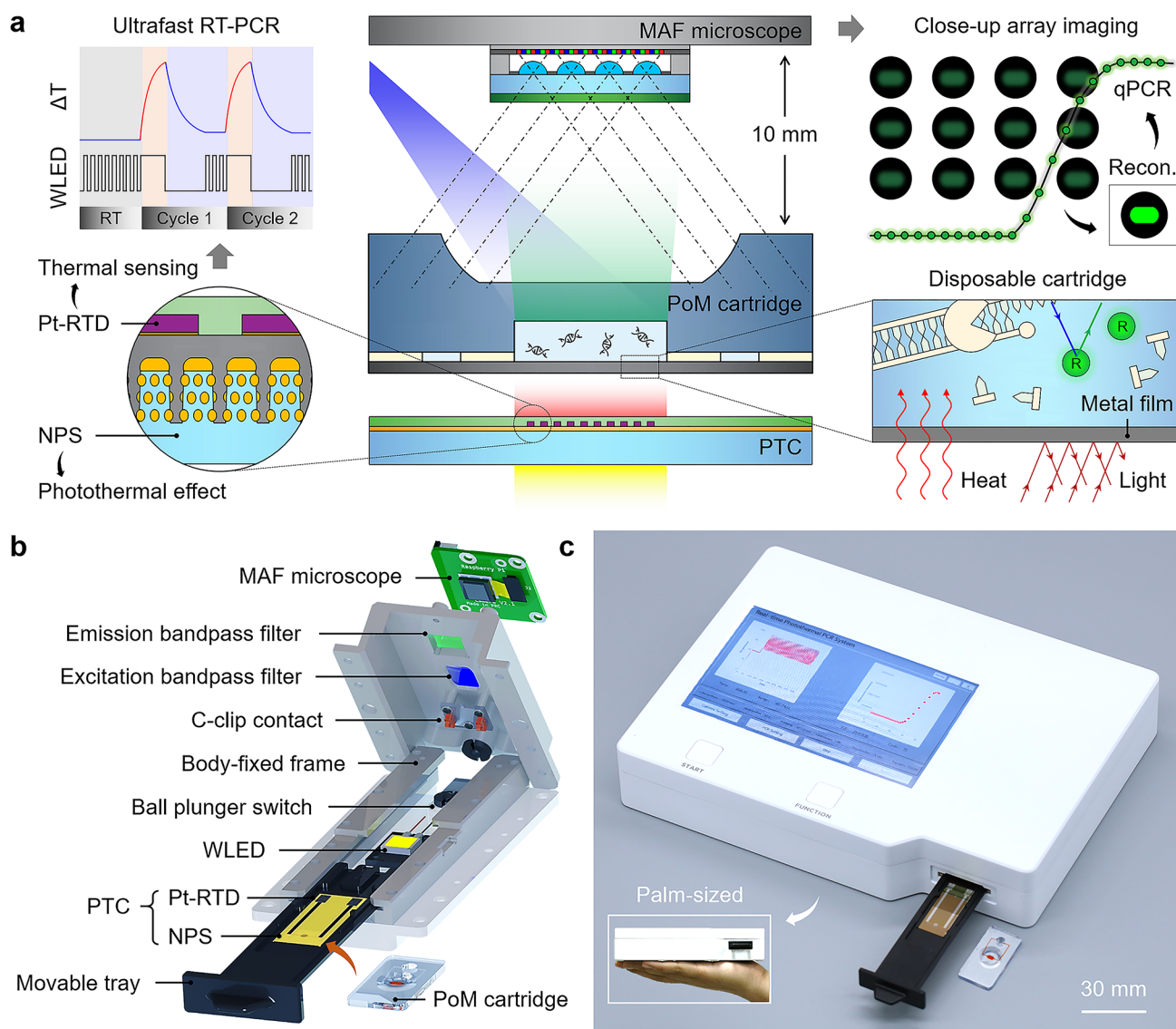
Figure 1. Plasmonic real-time RT-PCR (pRT-qPCR) system for decentralized testing. (a) Working principle for rapid and quantitative nucleic acid amplification, including ultrafast plasmonic thermocycler (PTC), disposable plastic-on-metal thin-film (PoM) cartridge, and ultrathin microlens array fluorescence (MAF) microscope. Both the PTC and the PoM cartridge rapidly transfer photothermal heat for the RT-PCR and completely block WLED light for efficient real-time quantification. The MAF microscope offers close-up and high-contrast fluorescence imaging with small focal length and wide field-of-view. (b) Schematic illustration for main components and their configurations. (c) Captured photograph of a fully packaged pRT-qPCR system on a palm size, suitable to rapid point-of-care molecular diagnostics.

optical configuration for photothermal excitation.[25,26] However, these methods are still under development to increase the reusability of nanomaterials and the cost-effectiveness for the POC applications.[29]

The RT-PCR strategies for the POC testing also demand fluorescence-based real-time detection for a prompt and accurate estimation of target gene expression in a low viral load.[30,31] The plasmonic PCR techniques struggle with the spectral crosstalk between photothermal excitation and fluorescence emission, limiting their real-time quantification.[32,33] Recently, diverse quantitative methods such as wavelength division of excitation sources[17,18] or end-point detection after magnetic clearance of plasmonic nanoparticles[19−21] have been actively incorporated with the plasmonic PCR. However, they suffer from a limited use of diverse commercial fluorophores, undesired optical noises, and

time-consuming postamplification procedures. In addition, conventional real-time PCR systems at the POC level have technical challenges for blocking undesired optical noises and avoiding bulky and complicated optical configurations.[34−37] For instance, the photodetectors, including photodiodes and image sensors, require robust alignment and massive integration of optical elements for noise-free and highly selective fluorescence detection, which limits their portability.[38−40] Recently, microlens array configurations provide close-up and high-contrast imaging at a compact size by significantly reducing the total tract length but have not yet been utilized for the POC fluorescence applications.[41−43]

Here, we report an ultrafast and palm-size plasmonic real-time RT-PCR (pRT-qPCR) system for decentralized molecular diagnostic testing (Figure 1a). The pRT-qPCR system performs ultrafast plasmonic nucleic acid amplification in a
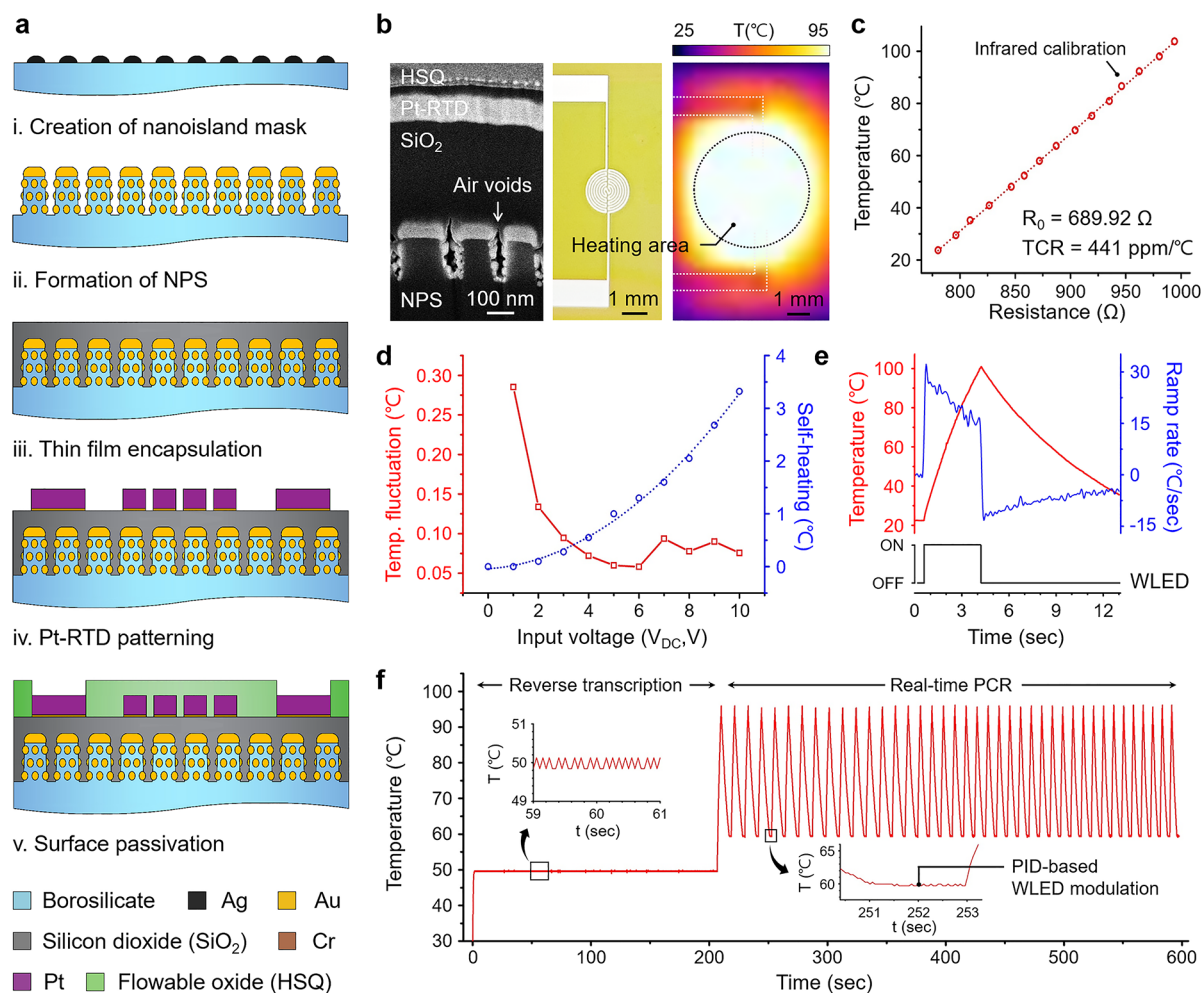
Figure 2. PTC for ultrafast PCR including nanoplasmonic substrate (NPS) and platinum resistance temperature detector (Pt-RTD). (a) Nanofabrication methods for the PTC, formed by using thermal dewetting, reactive ion etching, thermal evaporation, and metal lift-off. (b) FIB SEM, photograph and thermographic image of WLED-driven heating area on the PTC. (c) Pt-RTD calibration showing a strong linear relation between the surface temperature and the electrical resistance. (d) Optimal operating voltage for Pt-RTD showing minimum temperature fluctuation and self-heating. The operating voltage was selected at 3 V DC to minimize temperature sensing errors during photothermal heating. (e) Ramping curve and rate under the cyclic WLED illumination. (f) PID-controlled temperature profiles for isothermal reverse transcription at constant 50 °C and 40 PCR cycles repeating a single cycle of 95 °C for denaturation and 60 °C for annealing and extension in 10 s.

disposable plastic-on-metal thin film (PoM) cartridge and *in situ* quantification with an ultrathin microlens array fluorescence (MAF) microscope. The plasmonic thermocycler (PTC) combines a nanoplasmonic substrate (NPS) and platinum resistance temperature detector (Pt-RTD), which provide not only rapid and efficient conversion of white LED (WLED) light to heat but also direct and precise measurement of surface temperature. The PoM cartridge contains an injection-molded plastic chip and aluminum (Al) thin film, which facilitates rapid heat transfer, real-time quantification without spectral crosstalk, and permanent use of the PTC. The MAF microscope captures time-lapse microscopic images for real-time quantification at a short distance and allows high dynamic range (HDR) fluorescence detection after image reconstruction from the array images. This fully packaged system at a palm size finally demonstrates rapid real-time RT-PCR and *in situ* diagnostics of viral RNAs in COVID-19 patients with a short total assay time.

RESULTS AND DISCUSSION

The pRT-qPCR system fully integrates the PTC, PoM cartridge, MAF microscope, mechanical loading units, and fluorescence monitoring units into a single platform (Figures 1b and S1). The PoM cartridge is loaded on the body-fixed frame of a movable tray and tightly contacted with the PTC. The movable tray is manually mounted along a rail frame up to two ball plunger switches, which confirm the cartridge loading and then release the user lock for PCR operation. Two electrodes of the Pt-RTD on the PTC are mechanically coupled to a C-clip contact on the upper body-fixed frame and connected to the print circuit board (PCB) for resistance-based temperature detection. A high-powered WLED as a photothermal excitation source is located at a distance of 2.5 mm below the PTC. A blue LED (BLED) and an excitation bandpass filter are arranged at 60° relative to the detection path between the PoM cartridge and the MAF microscope for fluorescence imaging. The physical dimension of the pRT-qPCR system is 190 mm × 140 mm × 23 mm with a 580 g weight (Figure 1c and Supporting Information Video 1). All
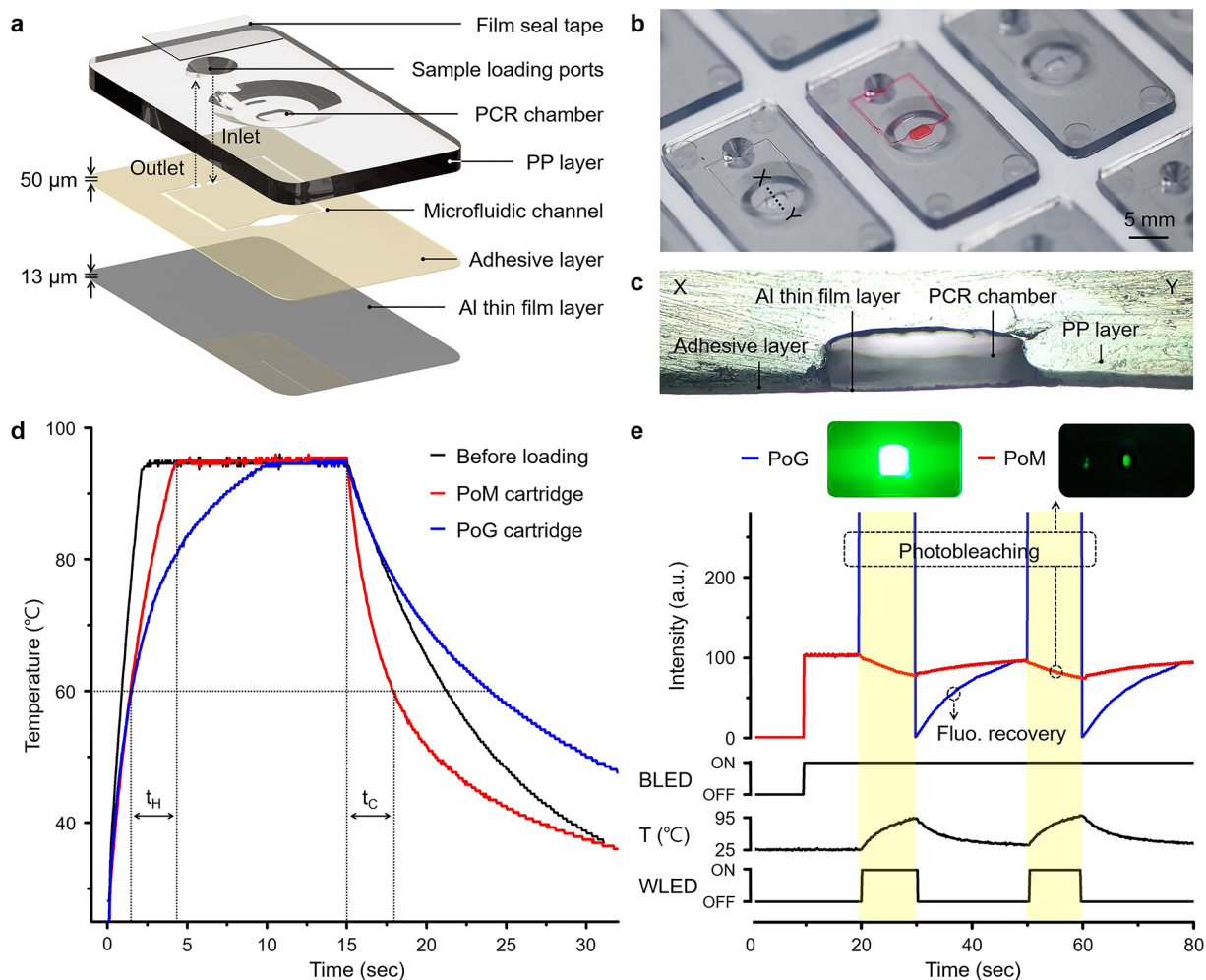
Figure 3. Disposable and low-cost PoM cartridge. (a) Schematic diagram of the PoM cartridge comprising polypropylene (PP) layer, 50 μm thick adhesive layer, and 13 μm thick aluminum (Al) thin film layer. (b) Optical photographs of the mass-produced PoM cartridge containing a 2 μL of sample volume. (c) Cross-sectional image along a line *XY*, which clearly shows the microfluidic PCR chamber. (d) Time response of photothermal heating and air cooling measured on unloaded PTC and those loaded with the PoM cartridge or a plastic-on-glass (PoG) cartridge. (e) Emitted fluorescence and temperature profiles of the PoG and PoM cartridges during the photothermal cycling. The PoM cartridge allows a faster ramping rate and *in situ* quantification without fluorescence loss.

functions such as plasmonic thermocycling, temperature monitoring, and fluorescence imaging are precisely controlled by a Raspberry Pi board. The embedded software automatically performs the diagnostic protocols and displays the analysis results on a liquid crystal display (LCD) screen. The internal product temperature is maintained below 30 °C through a plate-fin heat sink on the backside of the product and fan-based air circulation (Figure S2).

The PTC involves the wafer-level nanofabrication of NPS for a light-to-heat converter and Pt-RTD for a surface temperature monitor over a large area (Figure 2a). First, 180 nm high glass nanopillar arrays (GNAs) were formed on a borosilicate glass wafer by using reactive ion etching of thermally annealed silver nanoislands. Gold nanoislands (AuNIs) with diverse sizes and gaps were formed by using thermal evaporation of 40 nm thick Au layer across the top and sidewalls of the GNAs. A 500 nm thick silicon dioxide (SiO$_2$) was deposited using plasma-enhanced chemical vapor deposition (PECVD) to decrease the surface roughness of the NPS. A 100 nm thick Pt on the SiO$_2$-coated NPS was defined for RTD by using lift-off process and further annealed for 10 min at 200 °C. Note that the sheet resistance of the Pt-RTD is

decreased during the thermal annealing due to the increase in grain size, achieving a high temperature coefficient of resistance (TCR) and thermal stability during the PCR cycling (Figure S3). The Pt-RTD on the NPS was passivated with a 500 nm thick hydrogen silsesquioxane (HSQ) resist to prevent electrical contact with the PoM cartridge. The Pt electrodes were further coated with an electrically conductive epoxy adhesive to prevent mechanical scratch from the C-clip contact. Finally, the PTC was diced into 30 mm × 12 mm of 12 pieces from a single 4 in. wafer and placed on the movable tray for permanent use (Figure S4). The focused ion beam scanning electron microscopy (FIB SEM) of the PTC shows well-established NPS and Pt-RTD at the nanoscale (Figure 2b). The NPS strongly absorbs the full spectrum of visible light, rapidly converts into photothermal heat, and efficiently dissipates the heat through air voids in the nanopillar configuration (Figure S5). A spiral line pattern of the Pt-RTD with a length of 50 mm and a width of 100 μm is arranged in the center of the WLED-driven heating area. The resistive response of the Pt-RTD at different surface temperatures was measured by using an infrared thermographic camera with surface emissivity correction (Figure 2c). The measured
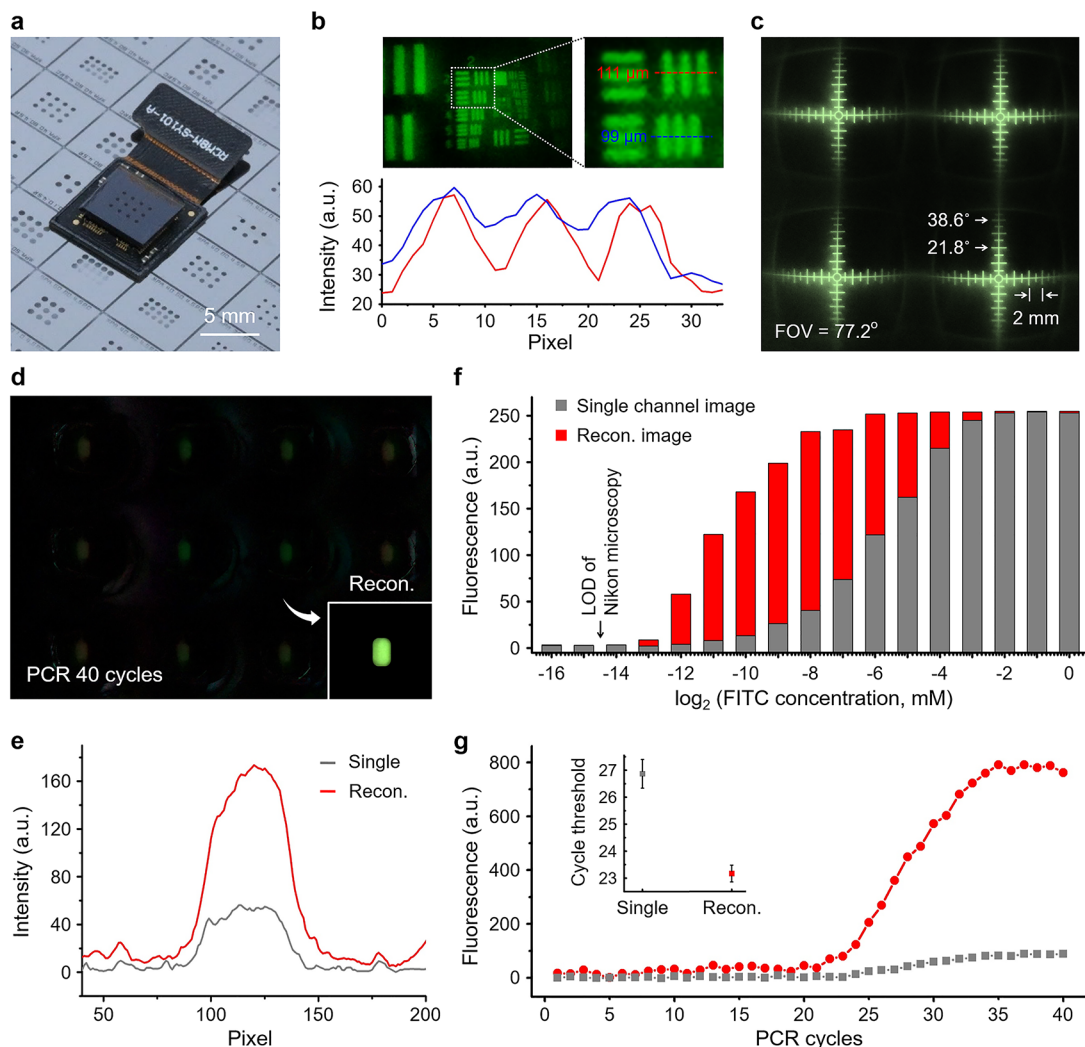
Figure 4. Ultrathin MAF microscope for close-up and high-contrast fluorescence imaging. (a) Captured photograph of the fully packaged MAF microscope containing 12 microlenses in 3 × 4 arrangement. (b) Captured images and the corresponding intensity profiles of USAF 1951 target with an object distance of 10 mm. The MAF microscope has the lateral resolution of 100 μm (group 2 element 3). (c) Field-of-view (FOV) measurement of the MAF microscope. The measured FOV of each microlens is 77.2°. (d) Captured array and reconstructed fluorescence images of the PCR mixtures after 40 PCR cycles in the PoM cartridge. The array images were reconstructed by using the image-averaging algorithm, the noise subtraction, and the image masking. (e) Corresponding intensity profiles in a single microlens and reconstructed images, which demonstrate substantial improvement in signal-to-noise ratio. (f) Limit of detection for FITC at nanomolar levels before and after the image reconstruction. (g) Amplification curves and cycle threshold values before and after the image reconstruction during the pRT-qPCR for 40 cycles.

nominal resistance is 689 Ω at 0 °C, which linearly increases with 441 ppm/°C of TCR value ranging to 100 °C. The local surface temperature was determined by the relative voltage value of the Pt-RTD (V_{RTD}) to the current sensing resistor (V_{REF}) under a constant input voltage (Figure S6). The magnitude of the input voltage source is derived from the temperature fluctuation and the self-heating of the Pt-RTD to affect the reliability of thermal sensing (Figure 2d). The temperature fluctuation error, i.e., the standard deviation of measured temperature values, is apparently reduced as the input voltage increases, however, causing critical self-heating errors generated from power dissipation in the Pt-RTD. The operating voltage at 3 V_{DC} clearly suppresses the temperature fluctuation error <0.1 °C as well as self-heating errors <0.5 °C. The Pt-RTD also interferes with accurate temperature monitoring of the NPS due to the intrinsic photothermal effect of Pt in visible wavelengths (Figure S7). However, the

transmitted light through the NPS was absorbed by the Pt-RTD and converted into a relatively small temperature increase of 3 °C, having little effect on the plasmonic thermocycling. As a result, the PTC demonstrates a significant correlation between the WLED illumination and the thermocycling with precise temperature monitoring (Figure 2e). The average heating and cooling rates between 60 and 95 °C were 18.85 and 8.89 °C/s, respectively. A two-step RT-PCR cycling (50 °C for RT, 95 °C for denaturation, and 60 °C for annealing and extension) was then performed by using the pRT-qPCR system (Figure 2f). The isothermal profiles for the complementary DNA (cDNA) synthesis and primer extension steps were acquired through the proportional-integral-derivative (PID) modulation of the WLED, which optimized the duty cycle and the light intensity and resulted in an accurate temperature correction (Figure S8). All the diagnostic protocols, including the RT process (210 s) and the

amplification process (400 s for 40 cycles) were successfully accomplished within 10 min.

The PoM cartridge exhibits high disposability and cost-effectiveness suitable for cost-effective POC testing. The cartridge configuration contains a polypropylene (PP) layer, an adhesive layer, and an Al thin film layer (Figures 3a and S9). The PP layer of 1.65 mm thickness retains a 200 μm thick PCR chamber and sample loading ports. The PCR samples are directly loaded with a micropipet into the inlet, gathered at the outlet adjacent to the inlet, and sealed together with a film seal tape to prevent water evaporation and cross-contamination during the whole PCR process. The adhesive layer of 50 μm thickness contains a polyethylene terephthalate film and double-sided acrylic adhesives, serving as a role for a microfluidic channel 300 μm in width. Finally, the adhesive layer was tightly attached to an Al thin film layer of 13 μm in thickness. The physical dimensions of the PoM cartridge are 15 mm × 28 mm × 1.71 mm. The PoM cartridges were batch-fabricated by using plastic injection molding and fine blanking techniques (Figure 3b). The captured cross-sectional image clearly indicates that the PCR chamber and microfluidic channel were successfully formed on the planar Al thin film layer (Figure 3c). The Al layer separates the PTC from the PCR mixtures and thus offers outstanding reusability of plasmonic nanostructures. In addition, the thin thickness and high thermal conductivity of the Al layer improve the ramping rate of PCR cycling. The measured times to heat up (t_H) and cool down (t_C) between 60 and 95 °C were compared for the unloaded PTC (before loading, black line), the PTC loaded with the PoM cartridge (PoM cartridge, red line), and the plastic-on-glass cartridge (PoG cartridge, blue line) (Figure 3d). The measured t_H are 1.4 and 2.7 s for the PTC under the unloaded and loaded PoM cartridge, respectively. For the experimental comparison, the PoM cartridge efficiently transfers heat from the PTC to the PCR mixtures by 2.9 times faster than the PoG cartridge. Moreover, the Al thin film layer exhibits a substantial improvement in the cooling rate with 2.2 times faster than the passive cooling of the PTCs and 3.2 times faster than the PoG cartridge. The rapid dissipation of photothermal energy through the Al layer was confirmed by using finite element analysis in COMSOL Multiphysics (Figure S10). Note that shortening of t_C leads to high amplification efficiency by preventing hybridization of single-stranded DNA before reaching the annealing temperature.[44] The PoM cartridge also provides in situ fluorescence detection of amplicons during the photothermal heating due to the high reflectivity of the Al layer. The emitted fluorescence signals from fluorescein isothiocyanate (FITC) were directly monitored in real time for the PoM and PoG cartridges during the plasmonic thermocycling to verify the spectral crosstalk between the WLED and fluorescence light (Figure 3e). Leaking WLED light from the plasmonic thermal cycler is transmitted through the bottom glass of the PoG cartridge and significantly delays the fluorescence recovery rate after photobleaching, disrupting fast fluorescence detection. However, the Al thin layer of the PoM cartridge completely blocks WLED light and effectively prevents photobleaching and photodamage of PCR components during the PCR reaction. Note that the fluorophores typically have a slight drop in the quantum yield with a temperature rise.[45] An antifouling surface treatment using ethanol cleaning and oxygen plasma was further performed on the PoM cartridge to prevent nonspecific adsorption of PCR components and bubble formation for high amplification efficiency. The water contact angles (θ) of the PP layer were measured after surface treatment for one month (Figure S11). The antifouling treatment clearly enhanced the surface energy of the PP layer to 22.5°, which kept it below 40° for one month. Sample preservation in the PoM cartridge during the plasmonic thermocycling was then verified for stability of PCR conditions (Figure S12). Microbubbles produced from the PCR reaction were guided and assembled at the top of the PCR chamber in the vertically standing PoM cartridge, which retained more than 80% of the sample after the plasmonic PCR with low bubble coverage, allowing stable fluorescence monitoring.

The fully packaged MAF microscope inside the pRT-qPCR system contains a commercial emission bandpass filter, inverted microlens arrays with a light absorber in a 3 × 4 arrangement, and a single CMOS imager (Figures 4a and S13). The total thickness of the microscope is 2.13 mm. The microlens arrays have a lens diameter of 300 μm, a focal length of 430 μm, and a pitch size of 800 μm to capture the whole area of the PCR chamber inside the PoM cartridge at a short object distance of 10 mm (Figure S14). The light absorber blocks the optical crosstalk between adjacent microlenses by highly absorbing visible wavelengths of light. The lateral resolution was measured from the fluorescence intensity profile by capturing a USAF 1951 target (Figure 4b). The single microlens image clearly distinguishes the line width of 99.2 μm (group 2 element 3), which is sufficient to observe the PCR chamber and the microchannels of the PoM cartridge. In addition, the MAF microscope shows a lateral resolution of 7 μm (group 6 element 2) at the contact position between the front window and the object (Figure S15). The field-of-view (FOV) of each microlens was then measured by capturing a grid target, resulting in wide FOV of 77.2° and the imaging area of 8 mm × 8 mm at the target distance of 10 mm (Figure 4c). The HDR fluorescence image was successfully achieved by using the image reconstruction algorithm including an image stacking, an image averaging, an image subtraction, and an image masking (Figures 4d and S16). The array fluorescence images were captured by using the MAF microscope for the PCR mixtures containing FAM-labeled TaqMan probes in the PoM cartridge after 40 plasmonic PCR cycles. The array images of individual microlenses were cropped for the image stacking and merged by using the image averaging tool in Chasys Draw IES, which reduces random background noises and improves the image contrast. The intensity profiles for the MAF image show that the image averaging process provides a high-contrast fluorescence image with a 1.33-fold improvement in signal-to-noise ratio (SNR)(Figure 4e). Note that the background noise is mostly caused by the reflection of excitation light from the Al layer and the diffraction from the PP layer. The reconstructed image was demonstrated by subtracting the merged image after plasmonic PCR from that of the initial state and extracting the fluorescence image of the PCR chamber. The image reconstruction completely reduces all the background noises by 98.69%, achieving reliable cyclic quantification during the PCR reaction. Finally, the MAF microscope demonstrates the limit-of-detection (LOD) for FITC dye in nanomolar concentration, comparable to a conventional fluorescence microscope (Figures 4f and S17). Note that FITC and FAM have identical spectral characteristics originating from fluorescein. The LOD of the MAF microscope was determined to be 123 nM, which is 2 times higher than that of the fluorescence microscope. The
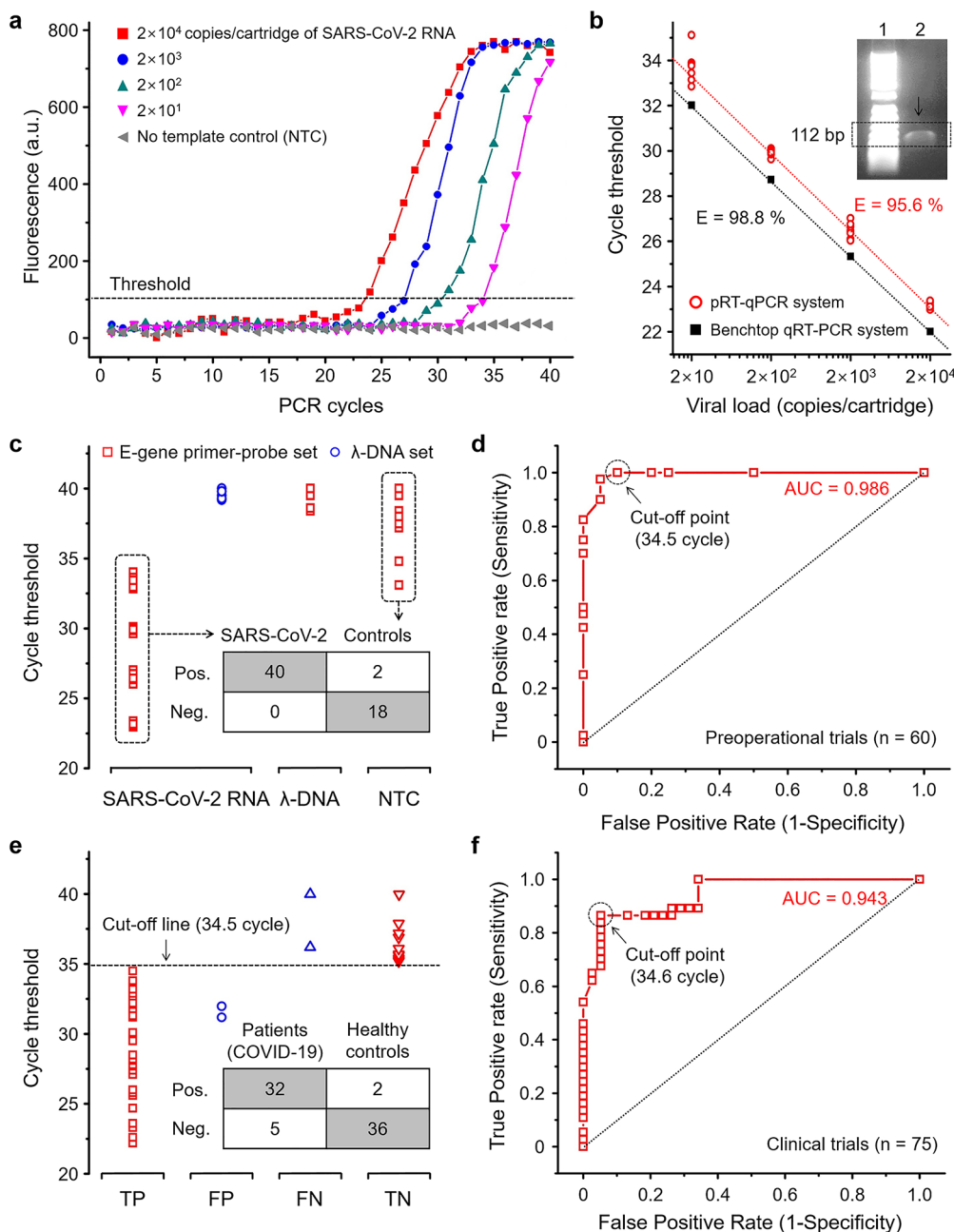
Figure 5. Molecular diagnostic test of COVID-19 disease using pRT-qPCR system. (a) Amplification curves of SARS-CoV-2 RNA samples during two-step RT-PCR (60−95 °C, 40 cycles) depending on the initial viral concentration. (b) Comparable amplification efficiencies between benchtop qRT-PCR and pRT-qPCR systems from standard curves of the cycle threshold versus the viral concentration. The agarose gel electrophoresis result clearly confirms the band for 112 bp target amplicons after pRT-qPCR. (c) Preoperational test results for the SARS-CoV-2 RNA and lambda DNAs (λ-DNA) samples of different targets and primer-probe set. (d) ROC curve for 40 SARS-CoV-2 samples and 20 controls. The AUC value and the cutoff value are 0.986 and 34.5 cycles, respectively. (e) Diagnostic test results for clinical samples of true positive (TP), false positive (FP), false negative (FN), and true negative (TN). (f) ROC curve for 37 patients with COVID-19 and 38 healthy controls with the AUC value of 0.943. The positive, negative, and total percent agreement is 87, 95, and 91%, respectively.

experimental results also indicate that the image reconstruction exhibits a substantial improvement of 16 times in fluorescence sensitivity. For instance, the pixel intensities in 2^{-10} mM concentration, i.e., 976 nM, from the single microlens and the reconstructed image and were 13.3 and 168, respectively. The highly sensitive detection at lower concentrations affects the cycle threshold (C_T) in real-time PCR (Figure 4g). An amplification curve for 40 cycles was performed by using the pRT-qPCR system, and the C_T value was determined as the crossing point with the threshold line at 5 times the standard

deviation of background fluorescence levels. As a result, the MAF microscope improves the LOD of fluorescence intensity and shortens the C_T values by about 4 cycles after the image reconstruction, comparable to conventional fluorescence microscopes.

Rapid amplification and real-time quantification of severe acute respiratory syndrome coronavirus 2 (SARS-CoV-2) have been finally demonstrated with the pRT-qPCR system. A 4 μL aliquot of PCR mixtures containing RNA templates, reaction buffer, enzyme buffer, forward/reverse primers, FAM-labeled

TaqMan probes, bovine serum albumin, and nuclease-free water were injected into the PoM cartridge (Table S1). The minimum concentration of RNA templates was 10^4 copies/mL, corresponding to 20 copies/2 μL for the PCR chamber. The pRT-qPCR test was automatically performed to amplify a target sequence of 112 base pairs (bp) after loading the PoM cartridge and assigning specific PCR conditions. The RT-PCR protocol was set at an initial RT of 50 °C for 5 min, followed by 40 cycles of denaturation at 95 °C for a holding time of 0 s and annealing/extension at 60 °C for 2 s. The array fluorescence images were captured with an exposure time of 1 s in each cycle at the annealing temperature and converted into normalized intensity for *in situ* quantification (Figure S18). The amplification curves follow a sigmoidal trend for different concentrations, indicating true exponential increases in the target amplicons above a threshold line (Figure 5a). No template control (NTC) tests show no amplification beyond the baseline fluorescence. A standard curve for the target concentrations versus the C_T values was further compared with a conventional benchtop qRT-PCR system (StepOnePlus Real-time PCR system, Thermo Fisher Scientific Inc.) (Figure 5b). The benchtop qRT-PCR system performed a two-step fast-mode PCR test (95 °C for 0 s and 60 °C for 10 s, ramping rate of 2.2 °C/s, total 60 min) for 20 μL of sample volume with the amplification efficiency of 98.8%. The pRT-qPCR system demonstrates high amplification efficiency of 95.6% with a slope of −3.43 even with the shorter annealing time and leads to the small difference of about 2 cycles in the C_T values compared to the benchtop qPCR system. Note that the small volume of PCR mixtures, 10 times lower than the benchtop qPCR system, and the high detection limits of the MAF microscope, 2 times higher than the fluorescence microscope, increase the C_T value in the amplification curve. The remaining solution including PCR products was extracted from the PoM cartridge by punching and pipetting via the Al thin layer, and verified by using gel electrophoresis; lane 1 for 50 bp DNA ladder and lane 2 for PCR products after the pRT-qPCR. The pRT-qPCR system clearly confirms the band for a 112 bp target amplicon in lane 2 with relatively low intensity due to the small extraction volume. The analytical specificity was then evaluated for SARS-CoV-2 RNA and lambda DNA (λ-DNA) with different templates and primer-probe sets (Figure 5c). The C_T values for the SARS-CoV-2 RNA and E gene set are significantly lower than those for the mismatches between templates and primer-probe sets. All viral strains are consequently identified without any cross-reaction of the interfering reagents. The preoperational trials (n = 40 for positive samples, and n = 20 for NTC) yield 100, 90, and 96.6% for the sensitivity, specificity, and accuracy, respectively. Note that high primer concentration for ultrafast RT-PCR may cause nonspecific amplification in the NTC reaction and lead to a decrease in the specificity; the concentrations of primer, probe, and polymerase would be further optimized for practical use. A receiver operating characteristic (ROC) curve analysis was also performed to determine the cutoff point for high classification performance (Figure 5d). The area under the ROC curve (AUC) is 0.986, comparable to the classification accuracy of a conventional real-time RT-PCR system. The cutoff point in C_T values was set to 34.5 cycles for the best positive predictive value to distinguish SARS-CoV-2 samples from the NTC and further utilized for following clinical test.

The ultrafast molecular diagnosis of the COVID-19 infection was finally performed to assess the clinical applicability of the pRT-qPCR system. The clinical samples were collected by using nasopharyngeal and oropharyngeal swabs from 37 infected patients of COVID-19 and 38 healthy controls. The COVID-19 infection status was confirmed in advance using a conventional benchtop qRT-PCR system after the purification of viral RNA from the clinical samples. The clinical diagnostic tests were conducted for 75 randomized samples by using the pRT-qPCR system with about 10 min per test (Figure 5e and Table S2). The C_T values from the unknown samples were successfully classified depending on the cutoff line for true positive (TP), false positive (FP), false negative (FN), and true negative (TN) groups. The positive, negative, and total percent agreements are 87, 95, and 91%, respectively. The cutoff value of 34.5 cycles clearly differentiates the patient samples from the healthy controls with high classification accuracy of over 90% in the clinical diagnostic trials. The two FP samples can be further separated from the positive diagnosis due to their nonsigmoidal amplification behavior for higher specificity. In addition, the ROC curve for the clinical test was constructed with an AUC value of 0.943 (Figure 5f). The optimal cutoff point in the clinical test was determined to be 34.6 cycles for the best predictive values, which shows a considerable match for that of the preoperational test. As a result, the pRT-qPCR system satisfies the POC requirement of time, cost, and size at the same time (Figure S19); it not only shows ultrafast molecular diagnostics 6 times faster than the conventional benchtop qPCR system but also exhibits a substantial improvement of 88 times in the package size as well as 41 times in the weight. Furthermore, the ultrafast and hand-held system achieves a good correlation with the benchtop qPCR system even with the short turnaround time and tightly meets the detailed criteria of target product profiles for the POC testing even outperforms competitive POC RT-PCR instruments and recent plasmonic PCR papers (Tables S3−S5).

CONCLUSIONS

In summary, this work has successfully demonstrated a decentralized biomedical diagnostic platform using the pRT-qPCR system for nanotechnology-driven ultrafast nucleic acid amplification and microtechnology-driven real-time fluorescence detection. The POC molecular diagnostic system consists of an ultrafast PTC, a cost-effective PoM cartridge, and a compact MAF microscope. The PTC contributes to a rapid response in both ramping up rate of 18.85 °C/s for photothermal heating and ramping down rate of 8.89 °C/s for passive cooling and direct surface temperature monitoring. The PoM cartridge increases the cooling rate by 2.2 times faster than the passive cooling and achieves *in situ* fluorescence detection without any spectral crosstalk during the WLED-driven plasmonic thermocycling. The MAF microscope captures close-up array fluorescence images of a tiny PCR chamber at such a short object distance of 10 mm and also enhances the detection limit by 16 times and the SNR by 1.33 times by the array image reconstruction. A fully packaged pRT-qPCR systems demonstrates rapid RT-PCR and real-time quantification of COVID-19 within 10 min, and exhibits affordable amplification efficiency (>95%), classification accuracy of preoperational test (>95%), and total percent agreement of clinical test (>90%). The pRT-qPCR system, with further technical developments, has much potential benefit for the clinical response to the pandemic at the POC level; microfluidic design for sufficient sample volume, reagent

optimization suitable for ultrafast amplification, and integration with extraction-free sample preparation methods. This decentralized platform can contribute to quality improvement in not only public health but also primary health care, and further provide the POC test for assorted diseases such as hepatitis, hospital-acquired infections, and sexually transmitted diseases.

EXPERIMENTAL SECTION

Preparation of PTC and PoM Cartridge. The NPS in the PTC was fabricated as previously described.[25,26] The HSQ (Fox-16, Dow Corning Corp.) was spin-coated at 4000 rpm for 30 s on the PTC to passivate the Pt-RTD. The electrically conductive epoxy adhesive (EO-21, Hightemp, Korea) was used to cover the Pt electrodes with a 100:4 mixing ratio of resin to hardener at 100 °C for 1 h. All the experimental data were acquired from one PTC, which showed long-term durability of at least 1000 RT-PCR tests without any loss of function. The PTC was integrated in the fully packaged pRT-qPCR system for permanent use, and only the PoM cartridge was used as disposable consumables. For the PoM cartridge, the Al thin film layer (A1050, LIB cathode foil for electronics, Sama Aluminum Co., Ltd.), the adhesive layer (DCA-93100H, Chemcos Co., Ltd.), and the film seal tape (Optical adhesive covers, Applied Biosystems) were prepared for handmade production. The Al layer and the adhesive layer were first adhered to a flat plate in order to prevent the Al thin film layer from warping and then precisely aligned with the PP layer. The plasma-Asher was used for oxygen plasma treatment after ethanol cleaning to increase the surface hydrophilicity of the PP layer with 270 W for 5 min. The ethanol cleaning of the PP layer converted it to a more hydrophobic surface by removing the impurities. The initial θ of the PP layer has a low surface energy of 78° close to the hydrophobicity and it was converted to 22.5°, which kept it for a month. The long-lasting hydrophilic properties exert a direct influence on the PCR efficiency inside the PoM cartridge. The PoM cartridge with all the surface treatment processes results in a higher end-point fluorescence intensity than the other conditions after the plasmonic PCR. The PoM cartridge provides a full guarantee of the high biocompatibility for a minimum of one month.

Temperature Calibration. The surface temperature of PTC was monitored and determined using an infrared (IR) thermographic camera (E75, FLIR Systems). The temperature value measured from the IR camera was first calibrated by a hot plate on the basis of surface emissivity correction of the PTC because the metal films reflect IR radiation. Then, the resistance shift of Pt-RTD during WLED modulation was calibrated with the average surface temperature in the area of the spiral resistance pattern from the IR camera.

Contact Angle Measurement. The degree of surface hydrophilicity or hydrophobicity was measured by a drop shape analyzer (EasyDrop FM40, KRUSS GmbH). The contact angle of a droplet on the Al thin layer or the PP layer was determined as the average value from 5 tests and observed for one month.

Microfabrication of MAF Microscope. The MAF microscope was fabricated as previously described.[43] The wafer-level microfabrication of the MAF microscope was done by integrating a metal−insulator−metal (MIM) light absorber and microlens arrays. DNR photoresist (DNR L300-D1, Dong-jin Semichem, Dong-jin, Korea) was patterned and then deposited by a 5 nm thick chrome (Cr) thin film. After the thin Cr lift-off, the 95 nm thick SiO₂ was deposited using PECVD. The MIM structure (Cr−SiO₂−Cr) was defined by a 100 nm thick Cr lift-off for highly absorbing the visible wavelengths of light and blocking optical crosstalk between adjacent microlenses. The DNR microlens arrays were further formed on the light absorber by using the DNR patterning, hydrophobic coating, and thermal reflow. The DNR microlens arrays were optimized with a lens diameter of 300 μm, a focal length of 430 μm, and a pitch size of 800 μm to fully image the PCR chamber of the PoM cartridge at a 10 mm object distance. The optical element was diced and placed on CMOS image sensor arrays (CMOS ISA, Sony IMX 219, 3280 × 2464 pixels) with 430 μm thick gap spacers.

MAF Image Reconstruction. The MAF image was acquired at each PCR cycle and transformed into the HDR single image after the RT-PCR process by using a series of image reconstruction protocols; array image slicing, image averaging, image subtraction, and image masking. (i) The array fluorescence image captured from the MAF microscope was cropped into 12 single channel images. (ii) The single channel images were stacked and merged by using the image averaging tools in Chasys Draw IES (ver. 5.23.01). (iii) The merged image after plasmonic PCR was subtracted from that of the initial state for reducing the background noise. (iv) The reconstructed image was finally achieved by using the image masking technique to extract the target fluorescence intensities from only the PCR chamber of the PoM cartridge. (v) The reconstructed images in every PCR cycle were converted into numerical values as the sum of pixel intensities. All the image reconstruction steps were performed in a minute using MATLAB software except for the image averaging.

Device Configuration of pRT-qPCR System. The WLED (LUXEON 7070, L170-5080701200000, Lumileds) was used for the photothermal excitation source with a power per unit area of 168 mW/mm² and the BLED (LXML-PR02-A900, Lumileds) for the fluorescence excitation source. The excitation bandpass filter (ET480/40x, Chroma Technology Corp.) was diced to 7.5 × 5 mm and arranged perpendicular to the BLED. The angle of incidence was determined at 30° to excite the TaqMan probes in the PoM cartridge at a short object distance. The emission bandpass filter (ET520/20m, Chroma Technology Co.) was diced to 7.5 mm × 7.5 mm to cover all microlens arrays and precisely placed in the front glass window of the MAF microscope. The movable tray (Al alloy, AL6061) with the PTC and the PoM cartridge inserted was operated along the rail by hand. The movable tray at complete insertion was in contact with the ball-plunger switch (FBPJS5, Woojin LM bearing) and the electrodes of PTC with a C-clip contact (PMT-1048, KH Electronics, Inc.). The single-board computer (Raspberry Pi 4 Model B, Raspberry Pi Foundation) managed all operations involving the pulse-width modulation of WLED and BLED, the resistance-based temperature reading, and the array fluorescence imaging. The cooling fan was attached to a Raspberry Pi for air circulation. The embedded software program was controlled by the touch panel of the liquid crystal display (5 in. capacitive touch display for Raspberry Pi, 800 × 480, Waveshare Electronics). All optoelectronic components were encapsulated in a custom-made plastic housing (acrylonitrile butadiene styrene, ABS).

Preparation of Plasmonic PCR Mixtures. The plasmonic PCR mixtures containing 4 μL of target viral RNA, 4 μL of 5× DF reaction buffer (optimized blend of Mg²⁺, dUTP, and dNTP, DirectFast qRT-PCR kit, NanoHelix Co., Ltd.), 2 μL of 10× DF enzyme buffer (optimized blend of reverse transcriptase, antibody-coupled Taq DNA polymerase, RNase inhibitor and heat-labile uracil-DNA-glycosylase, DirectFast qRT-PCR kit, NanoHelix Co., Ltd.), 1 μL of forward primer (100 μM, E_Sarbeco_F1, Koma Biotech Inc.), 1 μL of reverse primer (100 μM, E_Sarbeco_R2, Koma Biotech Inc.), 1 μL of TaqMan probe (10 μM, E_Sarbeco_P1, Koma Biotech Inc.), and 2 μL of bovine serum albumin (10 μg/μL BSA, Sigma-Aldrich) were brought to 20 μL of RNase-free water. The NTC was prepared by substituting 1 μL of RNase water for the target RNA in the PCR mixtures. The RT process time was set to 210 s for a minimum condition of ultrafast molecular diagnosis. For more efficient amplification of target sequences, the hold time for the RT process as well as the annealing and extension processes is recommended to be increased sufficiently. The λ-DNA (48,502 bp, Roche Applied Science) was prepared with forward and reverse primer (oligonucleotide synthesis for target sequence of 98 bp, Bioneer Inc.), and TaqMan probe (oligonucleotide synthesis, BIONICS) for analytical specificity evaluation. The PCR mixtures of 1 μL including the target amplicons after pRT-qPCR was extracted from the Al thin layer of the PoM cartridge using a pipet and loaded onto 2% agarose gel after mixing with 9 μL of RNase-free water, 1.5 μL of 10× sample loading buffer (Takara Bio Inc.), and SYBR Safe DNA gel stain (BioAssay Co., Ltd.). The gel electrophoresis was demonstrated by using Mupid-2plus (Takara Bio Inc.) with a GeneRuler 50 bp DNA ladder (Thermo Fisher Scientific Inc.).

Clinical Diagnostic Test. The nasopharyngeal and oropharyngeal samples were provided by the U2 Clinical Laboratories (Jangwon Medical Foundation). The viral RNA of the COVID-19 disease was extracted and purified by using the QIAamp DSP Viral RNA Mini Kit (QIAGEN). The conventional RT-qPCR tests targeting the E gene, open reading frame 1 (ORF1) gene, and internal control (ribonuclease P; RNaseP) were performed with a STANDARD M nCoV real-time detection kit (SD Biosensor) for clinical diagnosis of COVID-19, and the remaining samples were collected for the clinical diagnostic test of the pRT-qPCR system. The patient samples and healthy controls are given identification numbers after a random arrangement and delivered under single-blind condition. The pRT-qPCR system performed E-gene-targeted clinical diagnostic tests and internal control on each PoM cartridge.

Statistical Analysis. All of the data are described as means ± standard deviations from at least five experiments. The threshold line in the amplification curve was determined as five times the standard deviation of background values.

ASSOCIATED CONTENT

Data Availability Statement

The experimental data to support the results are available in the manuscript and the Supporting Information. The raw data are available from the authors on reasonable request.

Ⓢ Supporting Information

The Supporting Information is available free of charge at https://pubs.acs.org/doi/10.1021/acsnano.2c11831.

> Schematic diagrams of plasmonic real-time RT-PCR system, characteristics of plasmonic thermocycler, characteristics of plastic-on-metal cartridge, characteristics of microlens array fluorescence microscope, reconstructed fluorescence images during PCR cycle, comparison graph for point-of-care implementation, table for agreement analysis between conventional real-time PCR test and plasmonic real-time RT-PCR test, primer/probe sequences, comparison between plasmonic real-time RT-PCR system and target product profile for point-of-care test, performance comparison table for point-of-care RT-PCR instrument, and detailed comparison with recent point-of-care implementations for plasmonic PCR (PDF)

> Video 1: Overall workflow of the fully packaged plasmonic real-time RT-PCR system including sample preparation, sample loading, cartridge loading, plasmonic nucleic acid amplification, real-time quantification (MOV)

AUTHOR INFORMATION

Corresponding Author

Ki-Hun Jeong − *Department of Bio and Brain Engineering, Korea Advanced Institute of Science and Technology (KAIST), Daejeon 34141, Republic of Korea; KAIST Institute for Health Science and Technology (KIHST), Korea Advanced Institute of Science and Technology (KAIST), Daejeon 34141, Republic of Korea;* ⊙ orcid.org/0000-0003-4799-7816; Phone: +82.42.350.4323; Email: kjeong@kaist.ac.kr

Authors

Byoung-Hoon Kang − *Department of Bio and Brain Engineering, Korea Advanced Institute of Science and Technology (KAIST), Daejeon 34141, Republic of Korea; KAIST Institute for Health Science and Technology (KIHST), Korea Advanced Institute of Science and Technology (KAIST), Daejeon 34141, Republic of Korea*

Kyung-Won Jang − *Department of Bio and Brain Engineering, Korea Advanced Institute of Science and Technology (KAIST), Daejeon 34141, Republic of Korea; KAIST Institute for Health Science and Technology (KIHST), Korea Advanced Institute of Science and Technology (KAIST), Daejeon 34141, Republic of Korea*

Eun-Sil Yu − *Department of Bio and Brain Engineering, Korea Advanced Institute of Science and Technology (KAIST), Daejeon 34141, Republic of Korea; KAIST Institute for Health Science and Technology (KIHST), Korea Advanced Institute of Science and Technology (KAIST), Daejeon 34141, Republic of Korea*

Hamin Na − *Department of Bio and Brain Engineering, Korea Advanced Institute of Science and Technology (KAIST), Daejeon 34141, Republic of Korea; KAIST Institute for Health Science and Technology (KIHST), Korea Advanced Institute of Science and Technology (KAIST), Daejeon 34141, Republic of Korea*

Yun-Jae Lee − *OSANG Healthcare Co., Ltd., Anyang-si, Gyeonggi-do 14040, Korea*

Woong-Yeol Ko − *OSANG Healthcare Co., Ltd., Anyang-si, Gyeonggi-do 14040, Korea*

NamHo Bae − *Center for Nano Bio Development, National NanoFab Center (NNFC), Daejeon 34141, Republic of Korea;* ⊙ orcid.org/0000-0003-2561-7739

Donggee Rho − *Center for Nano Bio Development, National NanoFab Center (NNFC), Daejeon 34141, Republic of Korea*

Complete contact information is available at:
https://pubs.acs.org/10.1021/acsnano.2c11831

Author Contributions

B.-H.K. and K.-H.J. conceived the idea and designed the all experiments. K.-W.J. designed and fabricated the MAF microscope. B.-H.K., E.-S.Y., and H.N. produced the PoM cartridge and prepared PCR mixtures. B.-H.K. and Y.-J.L. designed and packaged the pRT-qPCR system. B.-H.K. and W.-Y.K. prepared the clinical test. B.-H.K., N.H.B., and D.R. designed and mass-produced the PP and adhesive layers. B.-H.K. and K.-H.J. analyzed and wrote the manuscript. All authors reviewed the manuscript and approved the final version. B.-H.K. and K.-W.J. contributed equally to this work.

Notes

The authors declare no competing financial interest.

ACKNOWLEDGMENTS

REFERENCES

(1) Ferretti, L.; Wymant, C.; Kendall, M.; Zhao, L. L.; Nurtay, A.; Abeler-Dorner, L.; Parker, M.; Bonsall, D.; Fraser, C. Quantifying SARS-CoV-2 Transmission Suggests Epidemic Control with Digital Contact Tracing. *Science* **2020**, *368*, 619.

(2) Song, Q.; Sun, X.; Dai, Z.; Gao, Y.; Gong, X.; Zhou, B.; Wu, J.; Wen, W. Point-of-Care Testing Detection Methods for COVID-19. *Lab Chip* **2021**, *21*, 1634−1660.

(3) Choi, J. R. Development of Point-of-Care Biosensors for COVID-19. *Front Chem.* **2020**, *8*. DOI: 10.3389/fchem.2020.00517

(4) Dinnes, J.; Deeks, J. J.; Berhane, S.; Taylor, M.; Adriano, A.; Davenport, C.; Dittrich, S.; Emperador, D.; Takwoingi, Y.; Cunningham, J.; Beese, S.; Domen, J.; Dretzke, J.; Ferrante di Ruffano, L.; Harris, I. M.; Price, M. J.; Taylor-Phillips, S.; Hooft, L.; Leeflang, M. M.; McInnes, M. D.; et al. Rapid, Point-of-Care Antigen and Molecular-based Tests for Diagnosis of SARS-CoV-2 Infection. *Cochrane Database Syst. Rev.* **2021**, *3*, CD013705.

(5) Lee, S. H.; Park, S. M.; Kim, B. N.; Kwon, O. S.; Rho, W. Y.; Jun, B. H. Emerging Ultrafast Nucleic Acid Amplification Technologies for Next-Generation Molecular Diagnostics. *Biosens Bioelectron* **2019**, *141*, 111448.

(6) Li, S.; Huang, S.; Ke, Y.; Chen, H.; Dang, J.; Huang, C.; Liu, W.; Cui, D.; Wang, J.; Zhi, X.; Ding, X. A HiPAD Integrated with rGO/MWCNTs Nano-Circuit Heater for Visual Point-of-Care Testing of SARS-CoV-2. *Adv. Funct Mater.* **2021**, *31*, 2100801.

(7) Albert, E.; Torres, I.; Bueno, F.; Huntley, D.; Molla, E.; Fernandez-Fuentes, M. A.; Martinez, M.; Poujois, S.; Forque, L.; Valdivia, A.; Solano de la Asuncion, C.; Ferrer, J.; Colomina, J.; Navarro, D. Field Evaluation of a Rapid Antigen Test (Panbio (TM) COVID-19 Ag Rapid Test Device) for COVID-19 Diagnosis in Primary Healthcare Centres. *Clin Microbiol Infec* **2021**, *27*, 472.e7.

(8) Peeling, R. W.; Olliaro, P. L.; Boeras, D. I.; Fongwen, N. Scaling Up COVID-19 Rapid Antigen Tests: Promises and Challenges. *Lancet Infect Dis* **2021**, *21*, E290−E295.

(9) Yan, S.; Ahmad, K. Z.; Warden, A. R.; Ke, Y.; Maboyi, N.; Zhi, X.; Ding, X. One-Pot Pre-Coated Interface Proximity Extension Assay for Ultrasensitive Co-Detection of Anti-SARS-CoV-2 Antibodies and Viral RNA. *Biosens Bioelectron* **2021**, *193*, 113535.

(10) Won, J.; Lee, S.; Park, M.; Kim, T. Y.; Park, M. G.; Choi, B. Y.; Kim, D.; Chang, H.; Kim, V. N.; Lee, C. J. Development of a Laboratory-Safe and Low-Cost Detection Protocol for SARS-CoV-2 of the Coronavirus Disease 2019 (COVID-19). *Exp Neurobiol* **2020**, *29*, 107−119.

(11) Kang, T. J.; Lu, J. M.; Yu, T.; Long, Y.; Liu, G. Z. Advances in Nucleic Acid Amplification Techniques (NAATs): COVID-19 Point-of-Care Diagnostics as an Example. *Biosens. Bioelectron.* **2022**, *206*, 114109.

(12) Valera, E.; Jankelow, A.; Lim, J.; Kindratenko, V.; Ganguli, A.; White, K.; Kumar, J.; Bashir, R. COVID-19 Point-of-Care Diagnostics: Present and Future. *ACS Nano* **2021**, *15*, 7899−7906.

(13) Sreejith, K. R.; Ooi, C. H.; Jin, J.; Dao, D. V.; Nguyen, N. T. Digital Polymerase Chain Reaction Technology - Recent Advances and Future Perspectives. *Lab Chip* **2018**, *18*, 3717−3732.

(14) Dong, X.; Liu, L.; Tu, Y.; Zhang, J.; Miao, G.; Zhang, L.; Ge, S.; Xia, N.; Yu, D.; Qiu, X. Rapid PCR Powered by Microfluidics: A Quick Review Under the Background of COVID-19 Pandemic. *Trends Analyt Chem.* **2021**, *143*, 116377.

(15) Roche, P. J. R.; Najih, M.; Lee, S. S.; Beitel, L. K.; Carnevale, M. L.; Paliouras, M.; Kirk, A. G.; Trifiro, M. A. Real Time Plasmonic qPCR: How Fast is Ultra-Fast? 30 Cycles in 54 Seconds. *Analyst* **2017**, *142*, 1746−1755.

(16) Kim, J.; Kim, H.; Park, J. H.; Jon, S. Gold Nanorod-based Photo-PCR System for One-Step, Rapid Detection of Bacteria. *Nanotheranostics* **2017**, *1*, 178−185.

(17) Mohammadyousef, P.; Paliouras, M.; Trifiro, M. A.; Kirk, A. G. Plasmonic and Label-Free Real-Time Quantitative PCR for Point-of-Care Diagnostics. *Analyst* **2021**, *146*, 5619−5630.

(18) Lee, J. H.; Cheglakov, Z.; Yi, J.; Cronin, T. M.; Gibson, K. J.; Tian, B.; Weizmann, Y. Plasmonic Photothermal Gold Bipyramid Nanoreactors for Ultrafast Real-Time Bioassays. *J. Am. Chem. Soc.* **2017**, *139*, 8054−8057.

(19) Jiang, K. L.; Wu, J. R.; Qiu, Y. W.; Go, Y. Y.; Ban, K.; Park, H. J.; Lee, J. H. Plasmonic Colorimetric PCR for Rapid Molecular Diagnostic Assays. *Sensor Actuat B-Chem.* **2021**, *337*, 129762.

(20) Cheong, J.; Yu, H.; Lee, C. Y.; Lee, J. U.; Choi, H. J.; Lee, J. H.; Lee, H.; Cheon, J. Fast Detection of SARS-CoV-2 RNA *via* the Integration of Plasmonic Thermocycling and Fluorescence Detection in a Portable Device. *Nat. Biomed Eng.* **2020**, *4*, 1159−1167.

(21) Wu, J. R.; Jiang, K. L.; Mi, H.; Qiu, Y. W.; Son, J.; Park, H. J.; Nam, J. M.; Lee, J. H. A Rapid and Sensitive Fluorescence Biosensor Based on Plasmonic PCR. *Nanoscale* **2021**, *13*, 7348−7354.

(22) Blumenfeld, N. R.; Bolene, M. A. E.; Jaspan, M.; Ayers, A. G.; Zarrandikoetxea, S.; Freudman, J.; Shah, N.; Tolwani, A. M.; Hu, Y.; Chern, T. L.; Rogot, J.; Behnam, V.; Sekhar, A.; Liu, X.; Onalir, B.; Kasumi, R.; Sanogo, A.; Human, K.; Murakami, K.; Totapally, G. S.; et al. Multiplexed Reverse-Transcriptase Quantitative Polymerase Chain Reaction Using Plasmonic Nanoparticles for Point-of-Care COVID-19 Diagnosis. *Nat. Nanotechnol* **2022**, *17*, 984−992.

(23) Son, J. H.; Cho, B.; Hong, S.; Lee, S. H.; Hoxha, O.; Haack, A. J.; Lee, L. P. Ultrafast Photonic PCR. *Light-Sci. Appl.* **2015**, *4*, e280.

(24) Son, J. H.; Hong, S. G.; Haack, A. J.; Gustafson, L.; Song, M. S.; Hoxha, O.; Lee, L. P. Rapid Optical Cavity PCR. *Adv. Healthc Mater.* **2016**, *5*, 167−174.

(25) Lee, Y.; Kang, B. H.; Kang, M.; Chung, D. R.; Yi, G. S.; Lee, L. P.; Jeong, K. H. Nanoplasmonic On-Chip PCR for Rapid Precision Molecular Diagnostics. *Acs Appl. Mater. Inter* **2020**, *12*, 12533−12540.

(26) Kang, B. H.; Lee, Y.; Yu, E. S.; Na, H. M.; Kang, M.; Huh, H. J.; Jeong, K. H. Ultrafast and Real-Time Nanoplasmonic On-Chip Polymerase Chain Reaction for Rapid and Quantitative Molecular Diagnostics. *ACS Nano* **2021**, *15*, 10194−10202.

(27) Monshat, H.; Wu, Z. W.; Pang, J. J.; Zhang, Q. J.; Lu, M. Integration of Plasmonic Heating and On-Chip Temperature Sensor for Nucleic Acid Amplification Assays. *Journal of Biophotonics* **2020**, *13*, e202000060.

(28) You, M.; Li, Z.; Feng, S.; Gao, B.; Yao, C.; Hu, J.; Xu, F. Ultrafast Photonic PCR Based on Photothermal Nanomaterials. *Trends Biotechnol* **2020**, *38*, 637−649.

(29) El-Atab, N.; Mishra, R. B.; Hussain, M. M. Toward Nanotechnology-Enabled Face Masks Against SARS-CoV-2 and Pandemic Respiratory Diseases. *Nanotechnology* **2022**, *33*, 062006.

(30) Lee, J.; Song, J. U.; Shim, S. R. Comparing the Diagnostic Accuracy of Rapid Antigen Detection Tests to Real Time Polymerase Chain Reaction in the Diagnosis of SARS-CoV-2 Infection: A Systematic Review and Meta-Analysis. *J. Clin Virol* **2021**, *144*, 104985.

(31) Rabaan, A. A.; Tirupathi, R.; Sule, A. A.; Aldali, J.; Mutair, A. A.; Alhumaid, S.; Muzaheed; Gupta, N.; Koritala, T.; Adhikari, R.; Bilal, M.; Dhawan, M.; Tiwari, R.; Mitra, S.; Emran, T. B.; Dhama, K. Viral Dynamics and Real-Time RT-PCR Ct Values Correlation with Disease Severity in COVID-19. *Diagnostics* **2021**, *11*, 1091.

(32) Morozov, V. N.; Kolyvanova, M. A.; Dement'eva, O. V.; Rudoy, V. M.; Kuzmin, V. A. Fluorescence Superquenching of SYBR Green I in Crowded DNA by Gold Nanoparticles. *J. Lumin.* **2020**, *219*, 116898.

(33) Walsh, T.; Lee, J.; Park, K. Laser-Assisted Photothermal Heating of a Plasmonic Nanoparticle-Suspended Droplet in a Microchannel. *Analyst* **2015**, *140*, 1535−1542.

(34) Li, Z. D.; Bai, Y. M.; You, M. L.; Hu, J.; Yao, C. Y.; Cao, L.; Xu, F. Fully Integrated Microfluidic Devices for Qualitative, Quantitative and Digital Nucleic Acids Testing at Point of Care. *Biosens. Bioelectron.* **2021**, *177*, 112952.

(35) Zhu, H. L.; Zhang, H. Q.; Ni, S.; Korabecna, M.; Yobas, L.; Neuzil, P. The Vision of Point-of-Care PCR Tests for the COVID-19 Pandemic and Beyond. *Trac-Trend Anal Chem.* **2020**, *130*, 115984.

(36) Capitan-Vallvey, L. F.; Palma, A. J. Recent Developments in Handheld and Portable Optosensing-a Review. *Anal. Chim. Acta* **2011**, *696*, 27−46.

(37) Shin, Y. H.; Gutierrez-Wing, M. T.; Choi, J. W. Review-Recent Progress in Portable Fluorescence Sensors. *J. Electrochem. Soc.* **2021**, *168*, 017502.

(38) Ahrberg, C. D.; Ilic, B. R.; Manz, A.; Neuzil, P. Handheld Real-Time PCR Device. *Lab Chip* **2016**, *16*, 586−92.

(39) Xiang, Q.; Xu, B.; Li, D. Miniature Real Time PCR on Chip with Multi-Channel Fiber Optical Fluorescence Detection Module. *Biomed Microdevices* **2007**, *9*, 443−9.

(40) Zhang, D.; Liu, Q. Biosensors and Bioelectronics on Smartphone for Portable Biochemical Detection. *Biosens Bioelectron* **2016**, *75*, 273−84.

(41) Kim, K.; Jang, K. W.; Ryu, J. K.; Jeong, K. H. Biologically Inspired Ultrathin Arrayed Camera for High-Contrast and High-Resolution Imaging. *Light Sci. Appl.* **2020**, *9*, 28.

(42) Jang, K. W.; Kim, K.; Bae, S. I.; Jeong, K. H. Biologically Inspired Ultrathin Contact Imager for High-Resolution Imaging of Epidermal Ridges on Human Finger. *Adv. Mater. Technol.* **2021**, *6*, 3200090.

(43) Bae, S. I.; Lee, S.; Kwon, J. M.; Kim, H. K.; Jang, K. W.; Lee, D.; Jeong, K. H. Machine-Learned Light-Field Camera that Reads Facial Expression from High-Contrast and Illumination Invariant 3D Facial Images. *Adv. Intell Syst-Ger* **2022**, *4*, 2100182.

(44) Wittwer, C. T.; Fillmore, G. C.; Garling, D. J. Minimizing the Time Required for DNA Amplification by Efficient Heat-Transfer to Small Samples. *Anal. Biochem.* **1990**, *186*, 328−331.

(45) Marras, S. A. Selection of Fluorophore and Quencher Pairs for Fluorescent Nucleic Acid Hybridization Probes. *Methods Mol. Biol.* **2006**, *335*, 3−16.